Optics and Lasers in Engineering 120 (2019) 49–58

Contents lists available at ScienceDirect

Optics and Lasers in Engineering

journal homepage: www.elsevier.com/locate/optlaseng

Review

Subaperture stitching testing for fine flat mirrors with large apertures using an orthonormal polynomial fitting algorithm

Lisong Yan[a,*], Wang Luo[c], Gongjing Yan[c], Xiaokun Wang[d], Haidong Zhang[d], Lianying Chao[a], Donglin Ma[a], Xiahui Tang[a,b]

[a] School of Optical and Electronic Information, Huazhong University of Science and Technology, Wuhan 430074, China
[b] Shenzhen Huazhong University of Science and Technology Research Institute, Shenzhen 518057, China
[c] Qiqihar University, Qiqihar 161000, China
[d] Key Laboratory of Optical System Advanced Manufacturing Technology, Changchun Institute of Optics, Fine Mechanics and Physics, Chinese Academy of Sciences, Changchun 130033, China

ARTICLE INFO

Keywords:
Interferometry
Flat surfaces
Stitching
Orthonormal polynomial

ABSTRACT

Interferometry, which measures the difference between a reference surface and a test surface, is widely used in high-precision testing. Usually the reference surface is considered as perfect and the surface errors there can be ignored during the testing. Considering the interferometry for fine optics with large apertures where the error of the reference surface is non-ignorable, we propose a stitching algorithm based on an orthonormal polynomial fitting method that can be used to accomplish the testing of both the reference surface and the surface under test simultaneously. To evaluate the accuracy of the above algorithm, the performance of the proposed method was analyzed by testing the tertiary mirror for the Thirty-Meter Telescope project (TMT project) and utilizing the algorithm in the simulation. Further, a practical experiment was implemented to demonstrate the practicability of the proposed method.

1. Introduction

In recent years, large aperture telescopes are being built all around the world, such as the TMT (Thirty-Meter Telescope) in Hawaii [1], EELT (European Extremely Large Telescope) in Chile [2] and LOT (Large Optical Telescope) in China [3]. As the aperture of the telescope increases, the size of the optical element also increases. In the design of TMT, the primary mirror is segmented into 492 aspherical mirrors 1.4 m in size [1]. For the tertiary mirror in the TMT design, an elliptical flat mirror with dimensions of 2.5 m × 3.5 m is applied, while in the recommended conceptual design for LOT, an elliptical flat mirror (1.573 m × 1.333 m) is proposed [3]. As the size of optical elements becomes larger, the need for precise and efficient measurement techniques is growing. Among these, a promising measurement method is subaperture stitching testing.

Subaperture stitching testing has been primarily developed for testing large-aperture optics, especially large flat mirrors, spherical surfaces with high numerical aperture, and large convex surfaces. Based on different shapes of the subaperture, annular subaperture stitching and circular stitching methods are proposed. The annular subaperture stitching method is an effective way to extend the vertical dynamic range of a conventional interferometer, but it can only accomplish measurements for rotationally symmetric aspheric surfaces [4–6]. The circular stitching method can test planes, spheres, and a variety of aspheres [7–9]. As the core of stitching testing, various stitching algorithms have been studied by many researchers. Among them, original algorithms such as the Kwon–Thunen method [10] or the simultaneous fitting method [11] use a series of global Zernike polynomials to accomplish the fitting of the test surfaces. Polynomial fitting methods suffer from localized irregularities in both the subaperture shape and the test surface shape. A discrete-type phase method was proposed by Stuhlinger to overcome the shortcomings of polynomial fitting methods [12]. In this method, the subaperture surface is represented by the phase value of a series of discrete points, and overlapping regions are required between adjacent subapertures. Relative adjustment errors such as piston and tip/tilt are calculated with the least squares method. The full aperture map can be obtained by applying adjustment errors between adjacent subapertures. This type of stitching has also been studied by other researchers [13–15]. Stitching testing can also be applied through non-null testing. The relative stitching algorithms are demonstrated in QED technology's patent [16] and other non-null stitching research work [17–19]. In interferometry, usually the figure error of the reference surface is treated as perfect. However, in high-accuracy stitching testing, the figure errors in the reference surface (which cannot be ignored) inherently create inconsistency between the overlapping data and appear as an important error source in each subaperture. One way to solve the problem is to calibrate the reference error before using it, which is usually difficult to realize because of

* Corresponding author.
E-mail address: yanlisong@hust.edu.cn (L. Yan).

https://doi.org/10.1016/j.optlaseng.2019.02.017
Received 15 January 2019; Received in revised form 21 February 2019; Accepted 26 February 2019
Available online 4 March 2019

the demands of high-accuracy auxiliary optical elements. The University of Arizona in the USA has provided a method based on maximum likelihood to accomplish the error separation between a reference surface in a 1 m aperture and a test surface in a 1.6 m aperture [20]. Aiming at improving the stitching accuracy for flat mirrors in large apertures and for separating the reference error from the test map, we propose a stitching algorithm which can be applied to stitching for a flat mirror with arbitrary shape. The advantages of the algorithm are evaluated and verified through simulations and experiments.

In this paper, we focus on the orthonormal polynomials fitting stitching algorithm and experimental demonstration of high accuracy surface measurement. The proposed stitching algorithm can be applied in the stitching testing for flat mirrors with arbitrary shape and it can reconstruct unknown surfaces including both the reference and the test simultaneously. To evaluate the performance of the above stitching algorithm, it has been applied to the M3 (the tertiary mirror in the Thirty-Meter telescope) simulation testing and a Φ300 mm standard surface testing experiment. The paper is organized as follows. In Section 2, the basic theory of the orthonormal polynomials fitting stitching algorithm is introduced. In Section 3, the effectiveness of our method is demonstrated through simulation testing of M3, which is an elliptical aperture mirror with dimensions of 2.5 m × 3.5 m. In Section 4, we demonstrate the performance of our stitching algorithm by testing a Φ300 mm standard surface. Finally, Section 5 provides conclusions.

2. Theory

The flow chart of the orthonormal polynomial fitting stitching algorithm is shown in Fig. 1. First, interferometric measurements were taken for each subaperture and all subaperture data were placed into a global coordinate system, which is defined beforehand according to their relative positions. Then basic polynomials were chosen to describe both the reference surface and the test surface. Considering that the shape of the test surface or the subaperture may be irregular, orthogonalization should be applied to each subaperture map of the test surface and the reference surface before the fitting calculation, as discussed in Section 2.1. After performing the orthogonalization, the orthonormal polynomials fitting calculation was performed, as discussed in Section 2.2. Then the fitting coefficients of the predefined polynomials, which are used to describe the surface maps of the reference and the test, were obtained and the relative surface maps were constructed. To get a better fitting result, residual maps of the reference surface and the test surface were calculated and the root mean square (RMS) of the residual maps were used to evaluate whether the fitting results meet the requirement. If not, basic polynomial terms were reselected and the polynomial fitting was recalculated until the residual maps met the requirement.

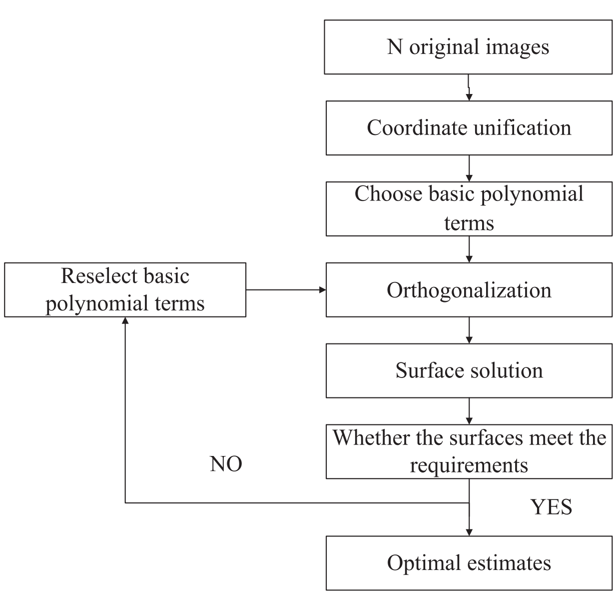

Fig. 1. Flow chart of the stitching algorithm.

2.1. Principles of orthonormal polynomials fitting

Optical systems or surfaces generally have a circular boundary. Zernike circle polynomials are widely used for wavefront analysis because of their orthogonality over a circular region and their representation of balanced classical aberrations.

However, for mirrors with a noncircular boundary, Zernike circular polynomials are neither orthogonal over such region nor do they represent balanced aberrations. Hence their special utility is lost and they should be expanded using an aberration function over a noncircular region [21, 22].

Considering a set of orthonormal polynomials $\{F_i\}$ over an arbitrary regionΣ, which can be expressed as a linear combination of Zernike polynomials$\{Z_i\}$, the relationship between them can be expressed as:

$$F_i = \sum_{j=1}^{J} M_{ij} Z_j \tag{1}$$

where M_{ij} is a conversion matrix and J is the number of predefined terms. As the Zernike polynomials are given beforehand, the orthonormal polynomials $\{F_i\}$ can be obtained if the conversion matrix M_{ij} is calculated.

Considering that the polynomials $\{F_i\}$ are orthogonal over the regionΣ, then

$$\left\langle F_i \mid F_j \right\rangle = \frac{\int_\Sigma F_i F_j dS}{\int_\Sigma dS} = \delta_{ij} \tag{2}$$

where δ_{ij} is the Kronecker delta.

Combining Eqs. (1) and (2), we obtain:

$$\left\langle Z_k \mid F_i \right\rangle = \sum_{j=1}^{J} \left\langle Z_k \mid Z_j \right\rangle [M_{ij}]^T \tag{3}$$

where i and k are the sequence numbers of polynomials $\{F_i\}$ and $\{Z_k\}$,$i, k = 1, 2, 3 \cdots J$ and $[M_{ij}]^T$ is the transpose matrix of the above conversion matrix with elements M_{ij}.

Eq. (3) can be expressed as:

$$C^{ZF} = C^{ZZ} {M_{ij}}^T \tag{4}$$

where both C^{ZF} and $C^{ZZ}$are $J \times J$ matrices respectively. The difference between them is that the inner element of C^{ZF} is the relationship of polynomials $\{Z_i\}$ and$\{F_i\}$, while the inner element of C^{ZZ} is the relationship of polynomials $\{Z_i\}$ and$\{Z_i\}$.

Similarly,

$$\left\langle F_i \mid F_k \right\rangle = \sum_{j=1}^{J} M_{ij} \left\langle Z_j \mid F_k \right\rangle = \delta_{ik} \tag{5}$$

As with Eq. (3), Eq. (5) can be written as:

$$M_{ij} C^{ZF} = I \tag{6}$$

where $I$is the unit matrix. Substituting Eq. (4) into Eq. (6), and defining

$$M = (Q^T)^{-1} \tag{7}$$

then

$$Q^T Q = C^{ZZ} \tag{8}$$

Eq. (8) can be solved for $Q$with the Cholesky decomposition [23] and the relative conversion matrix M_{ij} can be obtained, thus the relationship between the predefined Zernike polynomials$\{Z_i\}$ and the orthonormal polynomials $\{F_i\}$ over an arbitrary regionΣ is obtained, meaning that the orthonormal polynomials fitting is accomplished.

2.2. Stitching algorithm

For each subaperture testing map, the testing data can be expressed by Eq. (9) [20].

$$D_{ij} = D_{ij}^{\alpha} + residuals = a_{i1}Z_1(\rho_a, \theta_a + \varphi_{ai}) + a_{i2}Z_2(\rho_a, \theta_a + \varphi_{ai})$$
$$+a_{i3}Z_3(\rho_a, \theta_a + \varphi_{ai}) + a_{i4}Z_4(\rho_a, \theta_a + \varphi_{ai}) - \sum_{k=5}^{rm} a_{rk}Z_k(\rho_a, \theta_a + \varphi_{ai})$$
$$+\sum_{k=5}^{tm} a_{tk}Z_k(\rho_a, \theta_a + \varphi_{bi}) + residuals \tag{9}$$

whereD_{ij}: the testing phase data of point $j$in the *ith*subaperture;D_{ij}^{α}: the part of the data that can be described analytically by polynomials;*residuals*: the part of data that cannot be described by polynomials;

$$\begin{bmatrix} \sum_1 \phi_1 Z_1 \\ \sum_1 \phi_1 Z_2 \\ \sum_1 \phi_1 Z_3 \\ \sum_1 \phi_1 Z_4 \\ \sum_2 \phi_2 Z_1 \\ \sum_2 \phi_2 Z_2 \\ \sum_2 \phi_2 Z_3 \\ \sum_2 \phi_2 Z_4 \\ \vdots \\ \sum_{i=1}^N \phi_i Z_{t5} \\ \sum_{i=1}^N \phi_i Z_{t6} \\ \vdots \\ \sum_{i=1}^N \phi_i Z_{tm} \\ \sum_{i=1}^N \phi_i Z_{r5} \\ \sum_{i=1}^N \phi_i Z_{r6} \\ \vdots \\ \sum_{i=1}^N \phi_i Z_{rm} \end{bmatrix} = \left[\begin{array}{ccccccccccccccccc}
\sum_1 Z_1^2 & \sum_1 Z_1Z_2 & \sum_1 Z_1Z_3 & \sum_1 Z_1Z_4 & 0 & 0 & 0 & 0 & \cdots & \sum_1 Z_1Z_{t5} & \sum_1 Z_1Z_{t6} & \cdots & \sum_1 Z_1Z_{tm} & \sum_1 Z_1Z_{r5} & \sum_1 Z_1Z_{r6} & \cdots & \sum_1 Z_1Z_{rm} \\
\sum_1 Z_2Z_1 & \sum_1 Z_2^2 & \sum_1 Z_2Z_3 & \sum_1 Z_2Z_4 & 0 & 0 & 0 & 0 & \cdots & \sum_1 Z_2Z_{t5} & \sum_1 Z_2Z_{t6} & \cdots & \sum_1 Z_2Z_{tm} & \sum_1 Z_2Z_{r5} & \sum_1 Z_2Z_{r6} & \cdots & \sum_1 Z_2Z_{rm} \\
\sum_1 Z_3Z_1 & \sum_1 Z_3Z_2 & \sum_1 Z_3^2 & \sum_1 Z_3Z_4 & 0 & 0 & 0 & 0 & \cdots & \sum_1 Z_3Z_{t5} & \sum_1 Z_3Z_{t6} & \cdots & \sum_1 Z_3Z_{tm} & \sum_1 Z_3Z_{r5} & \sum_1 Z_3Z_{r6} & \cdots & \sum_1 Z_3Z_{rm} \\
\sum_1 Z_4Z_1 & \sum_1 Z_4Z_2 & \sum_1 Z_4Z_3 & \sum_1 Z_4^2 & 0 & 0 & 0 & 0 & \cdots & \sum_1 Z_4Z_{t5} & \sum_1 Z_4Z_{t6} & \cdots & \sum_1 Z_4Z_{tm} & \sum_1 Z_4Z_{r5} & \sum_1 Z_4Z_{r6} & \cdots & \sum_1 Z_4Z_{rm} \\
0 & 0 & 0 & 0 & \sum_2 Z_1^2 & \sum_2 Z_1Z_2 & \sum_2 Z_1Z_3 & \sum_2 Z_1Z_4 & \cdots & \sum_2 Z_1Z_{t5} & \sum_1 Z_1Z_{t6} & \cdots & \sum_2 Z_1Z_{tm} & \sum_2 Z_1Z_{r5} & \sum_2 Z_1Z_{r6} & \cdots & \sum_2 Z_1Z_{rm} \\
0 & 0 & 0 & 0 & \sum_2 Z_2Z_1 & \sum_2 Z_2^2 & \sum_2 Z_2Z_3 & \sum_2 Z_2Z_4 & \cdots & \sum_2 Z_2Z_{t5} & \sum_1 Z_2Z_{t6} & \cdots & \sum_2 Z_2Z_{tm} & \sum_2 Z_2Z_{r5} & \sum_2 Z_2Z_{r6} & \cdots & \sum_2 Z_2Z_{rm} \\
0 & 0 & 0 & 0 & \sum_2 Z_3Z_1 & \sum_2 Z_3Z_2 & \sum_2 Z_3^2 & \sum_2 Z_3Z_4 & \cdots & \sum_2 Z_3Z_{t5} & \sum_1 Z_3Z_{t6} & \cdots & \sum_2 Z_3Z_{tm} & \sum_2 Z_3Z_{r5} & \sum_2 Z_3Z_{r6} & \cdots & \sum_2 Z_3Z_{rm} \\
0 & 0 & 0 & 0 & \sum_2 Z_4Z_1 & \sum_2 Z_4Z_2 & \sum_2 Z_4Z_2 & \sum_2 Z_4^2 & \cdots & \sum_2 Z_4Z_{t5} & \sum_1 Z_4Z_{t6} & \cdots & \sum_2 Z_4Z_{tm} & \sum_2 Z_4Z_{r5} & \sum_2 Z_4Z_{r6} & \cdots & \sum_2 Z_4Z_{rm} \\
\vdots & \vdots & \vdots & \vdots & \vdots & \vdots & \vdots & \vdots & \ddots & \vdots & \vdots & \ddots & \vdots & \vdots & \ddots & \vdots & \\
\sum_1 Z_1Z_{t5} & \sum_1 Z_2Z_{t5} & \sum_1 Z_3Z_{t5} & \sum_1 Z_4Z_{t5} & \sum_2 Z_1Z_{t5} & \sum_2 Z_2Z_{t5} & \sum_2 Z_3Z_{t5} & \sum_2 Z_4Z_{t5} & \cdots & \sum_{i=1}^N Z_{t5}Z_{t5} & \sum_{i=1}^N Z_{t5}Z_{t6} & \cdots & \sum_{i=1}^N Z_{t5}Z_{tm} & \sum_{i=1}^N Z_{r5}Z_{t5} & \sum_{i=1}^N Z_{r6}Z_{t5} & \cdots & \sum_{i=1}^N Z_{rm}Z_{t5} \\
\sum_1 Z_1Z_{t6} & \sum_1 Z_2Z_{t6} & \sum_1 Z_3Z_{t6} & \sum_1 Z_4Z_{t6} & \sum_1 Z_1Z_{t6} & \sum_1 Z_2Z_{t6} & \sum_1 Z_3Z_{t6} & \sum_1 Z_4Z_{t6} & \cdots & \sum_{i=1}^N Z_{t6}Z_{t5} & \sum_{i=1}^N Z_{t6}Z_{t6} & \cdots & \sum_{i=1}^N Z_{t6}Z_{tm} & \sum_{i=1}^N Z_{r5}Z_{t6} & \sum_{i=1}^N Z_{r6}Z_{t6} & \cdots & \sum_{i=1}^N Z_{rm}Z_{t6} \\
\vdots & \vdots & \vdots & \vdots & \vdots & \vdots & \vdots & \vdots & \ddots & \vdots & \vdots & \ddots & \vdots & \vdots & \ddots & \vdots & \\
\sum_1 Z_1Z_{tm} & \sum_1 Z_2Z_{tm} & \sum_1 Z_3Z_{tm} & \sum_1 Z_4Z_{tm} & \sum_2 Z_1Z_{tm} & \sum_2 Z_2Z_{tm} & \sum_2 Z_3Z_{tm} & \sum_2 Z_4Z_{tm} & & \sum_{i=1}^N Z_{tm}Z_{t5} & \sum_{i=1}^N Z_{tm}Z_{t6} & & \sum_{i=1}^N Z_{tm}Z_{tm} & \sum_{i=1}^N Z_{r5}Z_{tm} & \sum_{i=1}^N Z_{r6}Z_{tm} & \cdots & \sum_{i=1}^N Z_{rm}Z_{tm} \\
\sum_1 Z_1Z_{r5} & \sum_1 Z_2Z_{r5} & \sum_1 Z_3Z_{r5} & \sum_1 Z_4Z_{r5} & \sum_2 Z_1Z_{r5} & \sum_2 Z_2Z_{r5} & \sum_2 Z_3Z_{r5} & \sum_2 Z_4Z_{r5} & \cdots & \sum_{i=1}^N Z_{r5}Z_{t5} & \sum_{i=1}^N Z_{r5}Z_{t6} & \cdots & \sum_{i=1}^N Z_{r5}Z_{tm} & \sum_{i=1}^N Z_{r5}Z_{r5} & \sum_{i=1}^N Z_{r5}Z_{r6} & \cdots & \sum_{i=1}^N Z_{r5}Z_{rm} \\
\sum_1 Z_1Z_{r6} & \sum_1 Z_2Z_{r6} & \sum_1 Z_3Z_{r6} & \sum_1 Z_4Z_{r6} & \sum_2 Z_1Z_{r6} & \sum_2 Z_2Z_{r6} & \sum_2 Z_3Z_{r6} & \sum_2 Z_4Z_{r6} & \ddots & \sum_{i=1}^N Z_{r6}Z_{t5} & \sum_{i=1}^N Z_{r6}Z_{t6} & \ddots & \sum_{i=1}^N Z_{r6}Z_{tm} & \sum_{i=1}^N Z_{r6}Z_{r5} & \sum_{i=1}^N Z_{r6}Z_{r6} & \cdots & \sum_{i=1}^N Z_{r6}Z_{rm} \\
\vdots & \vdots & \vdots & \vdots & \vdots & \vdots & \vdots & \vdots & \cdots & \vdots & \vdots & \cdots & \vdots & \vdots & \ddots & \vdots & \\
\sum_1 Z_1Z_{rm} & \sum_1 Z_2Z_{rm} & \sum_1 Z_3Z_{rm} & \sum_1 Z_4Z_{rm} & \sum_2 Z_1Z_{rm} & \sum_2 Z_2Z_{rm} & \sum_2 Z_3Z_{rm} & \sum_2 Z_4Z_{rm} & & \sum_{i=1}^N Z_{rm}Z_{t5} & \sum_{i=1}^N Z_{rm}Z_{t6} & & \sum_{i=1}^N Z_{rm}Z_{tm} & \sum_{i=1}^N Z_{rm}Z_{r5} & \sum_{i=1}^N Z_{rm}Z_{r6} & \cdots & \sum_{i=1}^N Z_{rm}Z_{rm}
\end{array}\right] \begin{bmatrix} a_{11} \\ a_{12} \\ a_{13} \\ a_{14} \\ a_{21} \\ a_{22} \\ a_{23} \\ a_{24} \\ \vdots \\ a_{t5} \\ a_{t6} \\ \vdots \\ a_{tm} \\ a_{r5} \\ a_{r6} \\ \vdots \\ a_{rm} \end{bmatrix} \tag{13}$$

Z_1, Z_2, Z_3, Z_4: the terms describing the phase errors introduced by the alignment, such as piston, x tilt, y tilt, and defocus;Z: polynomials used to represent the surfaces;i: the index of the subaperture;j: the index of the phase data;*rm, tm*: the index of terms used to describe the reference surface and testing surface, respectively;a_r, a_t: coefficients of the reference surface and the testing surface, respectively;ρ, θ, φ: global coordinates of reference and testing surfaces in a subaperture.

Because the testing map of each subaperture meets the Gauss distribution [20], the likelihood function of a subaperture testing map can be written as:

$$L(D_{ij}|a_i, a_r, a_t) = \frac{1}{(\sqrt{2\pi\sigma})^{Nv_i}} \exp(-\frac{1}{2\sigma^2}\sum_{i=1}^{N}\sum_{j=1}^{v_i}(D_{ij} - D_{ij}^{a})^2) \tag{10}$$

where N is the number of testing subapertures, v_i is the number of testing points in the *ith* subaperture, and σ is the standard deviation of the testing result.

The goal of the stitching algorithm is to maximize the likelihood function, which means that the value of the Eq. (11) should be minimized.

$$S = \sum_{i=1}^{N}\sum_{j=1}^{v_i}(D_{ij} - D_{ij}^{\alpha})^2 = \min \tag{11}$$

Calculate the partial derivative of Eq. (11) as shown in Eq. (12).

$$\begin{cases} \frac{\partial S}{\partial a_{i1}} = 0 \\ \frac{\partial S}{\partial a_{i2}} = 0 \\ \frac{\partial S}{\partial a_{i3}} = 0 \\ \frac{\partial S}{\partial a_{i4}} = 0 \\ \frac{\partial S}{\partial a_{rk}} = 0 \\ \frac{\partial S}{\partial a_{tk}} = 0 \end{cases} \tag{12}$$

Eq. (12) can be transformed to a group of linear equations in the following form, as shown in Eq. (13).

And Eq. (13) can be expressed as:

$$P = Q \cdot R \tag{14}$$

If we define the parameters according to the following Eqs. (15)–(24), then Eqs. (13) and (14) can be written as:

The final least-squares equation derived from Eq. (13) becomes

$$\begin{bmatrix} P_1 \\ P_2 \\ P_3 \\ \vdots \\ P_N \\ P_t \\ P_r \end{bmatrix} = \begin{bmatrix} Q_{11} & Q_{12} & Q_{13} & \cdots & Q_{1N} & Q_{1t} & Q_{1r} \\ Q_{21} & Q_{22} & Q_{23} & \cdots & Q_{2N} & Q_{2t} & Q_{2r} \\ Q_{31} & Q_{32} & Q_{33} & \cdots & Q_{3N} & Q_{3t} & Q_{3r} \\ \vdots & \vdots & \vdots & \ddots & \vdots & \vdots & \vdots \\ Q_{N1} & Q_{N2} & Q_{N3} & \cdots & Q_{NN} & Q_{Nt} & Q_{Nr} \\ Q_{t1} & Q_{t2} & Q_{t3} & \cdots & Q_{tN} & Q_{tt} & Q_{tr} \\ Q_{r1} & Q_{r2} & Q_{r3} & \cdots & Q_{rN} & Q_{rr} & Q_{rr} \end{bmatrix} \begin{bmatrix} R_1 \\ R_2 \\ R_3 \\ \vdots \\ R_N \\ R_t \\ R_r \end{bmatrix} \tag{15}$$

To better explain each term in Eq. (15), their detailed descriptions follow.

P is a vector with $[(rm + tm - 8) + 4N]$rows and it can be written as:

$$P_i = \begin{bmatrix} \sum_i \phi_i Z_1 \\ \sum_i \phi_i Z_2 \\ \sum_i \phi_i Z_3 \\ \sum_i \phi_i Z_4 \end{bmatrix} (i = 1 \cdots N) \; P_t = \begin{bmatrix} \sum_{i=1}^N \phi_i Z_{t5} \\ \sum_{i=1}^N \phi_i Z_{t6} \\ \vdots \\ \sum_{i=1}^N \phi_i Z_{tm} \end{bmatrix} P_r = \begin{bmatrix} \sum_{i=1}^N \phi_i Z_{r5} \\ \sum_{i=1}^N \phi_i Z_{r6} \\ \vdots \\ \sum_{i=1}^N \phi_i Z_{rm} \end{bmatrix} \tag{16}$$

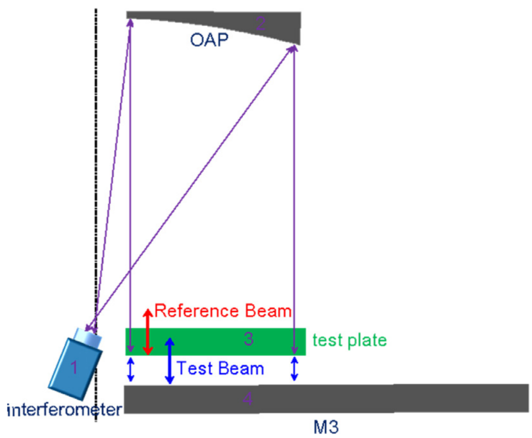

Fig. 2. Test setup.

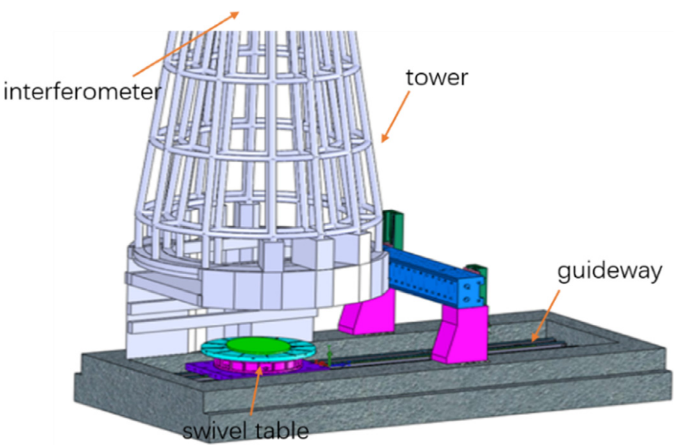

Fig. 3. Equipment of M3 testing.

Q is a matrix of size $[(rm + tm - 8) + 4N]$and the relationship of elements in it can be expressed with Eqs. (17)–(23).

$$Q_{ii} = \begin{bmatrix} \sum_i Z_1^2 & \sum_i Z_1 Z_2 & \sum_i Z_1 Z_3 & \sum_i Z_1 Z_4 \\ \sum_i Z_2 Z_1 & \sum_i Z_2^2 & \sum_i Z_2 Z_3 & \sum_i Z_2 Z_4 \\ \sum_i Z_3 Z_1 & \sum_i Z_3 Z_2 & \sum_i Z_3^2 & \sum_i Z_3 Z_4 \\ \sum_i Z_4 Z_1 & \sum_i Z_4 Z_2 & \sum_i Z_4 Z_3 & \sum_i Z_4^2 \end{bmatrix} (i = 1, 2 \cdots N) \tag{17}$$

$$Q_{ij} = \begin{bmatrix} 0 & 0 & 0 & 0 \\ 0 & 0 & 0 & 0 \\ 0 & 0 & 0 & 0 \\ 0 & 0 & 0 & 0 \end{bmatrix} (i, j = 1, 2 \cdots N, i \neq j) \tag{18}$$

Table 1
Parameters and errors in the testing.

Size of the reference surface	1.5 m diameter
Surface error of reference surface	RMS (Root Mean Square): 60.32 nm
Size of M3	2.5 m × 3.5 m elliptical aperture mirror
Surface error of M3	RMS: 116.05 nm
Alignment error in the radial directionρ	10 µm/m
Alignment error in the rotation directionθ	10″
Tip error in the X direction	0.5″
Tilt error in the Y direction	0.5″
Mechanical jump	10 µm
Random error in the map testing	RMS: 0.5 nm

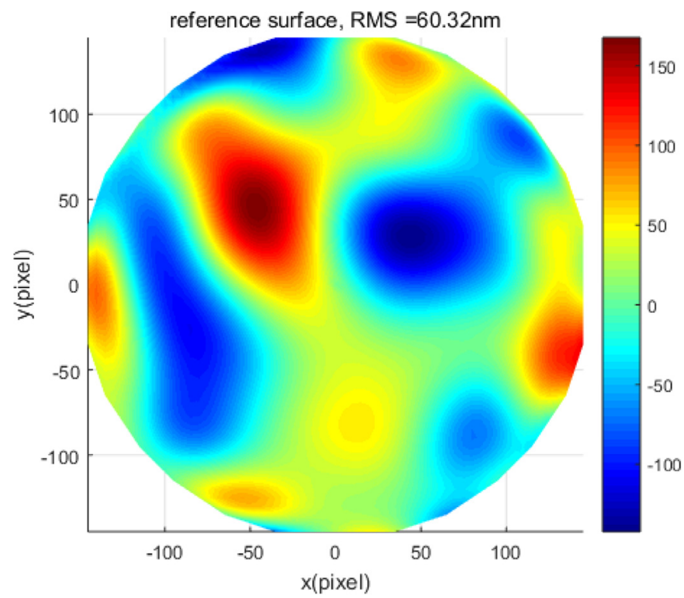

Fig. 4. Reference surface errors.

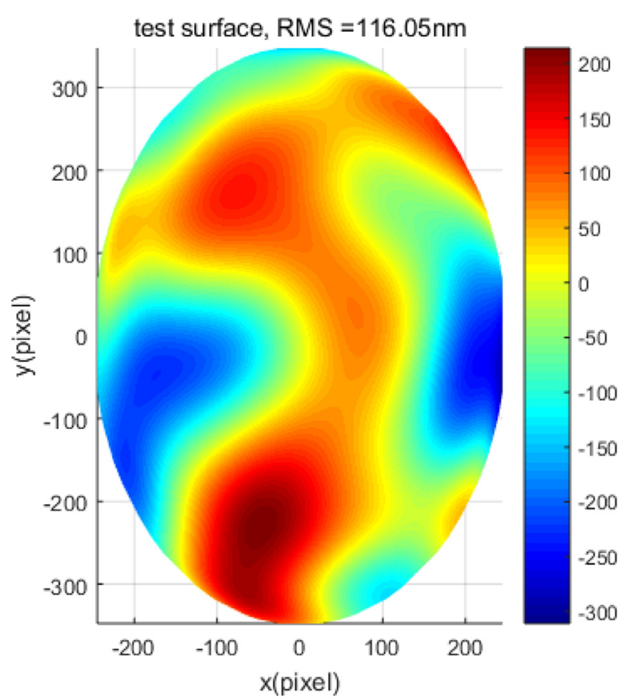

Fig. 5. M3 surface errors.

$$Q_{ti} = \begin{bmatrix} \sum_i Z_1 Z_{t5} & \sum_i Z_2 Z_{t5} & \sum_i Z_3 Z_{t5} & \sum_i Z_4 Z_{t5} \\ \sum_i Z_1 Z_{t6} & \sum_i Z_2 Z_{t6} & \sum_i Z_3 Z_{t6} & \sum_i Z_4 Z_{t6} \\ \vdots & \vdots & \vdots & \vdots \\ \sum_i Z_1 Z_{tm} & \sum_i Z_2 Z_{tm} & \sum_i Z_3 Z_{tm} & \sum_i Z_4 Z_{tm} \end{bmatrix} (i = 1, 2 \cdots N) \tag{19}$$

$$Q_{ri} = \begin{bmatrix} \sum_i Z_1 Z_{r5} & \sum_i Z_2 Z_{r5} & \sum_i Z_3 Z_{r5} & \sum_i Z_4 Z_{r5} \\ \sum_i Z_1 Z_{r6} & \sum_i Z_2 Z_{r6} & \sum_i Z_3 Z_{r6} & \sum_i Z_4 Z_{r6} \\ \vdots & \vdots & \vdots & \vdots \\ \sum_i Z_1 Z_{rm} & \sum_i Z_2 Z_{rm} & \sum_i Z_3 Z_{rm} & \sum_i Z_4 Z_{rm} \end{bmatrix} (i = 1, 2 \cdots N) \tag{20}$$

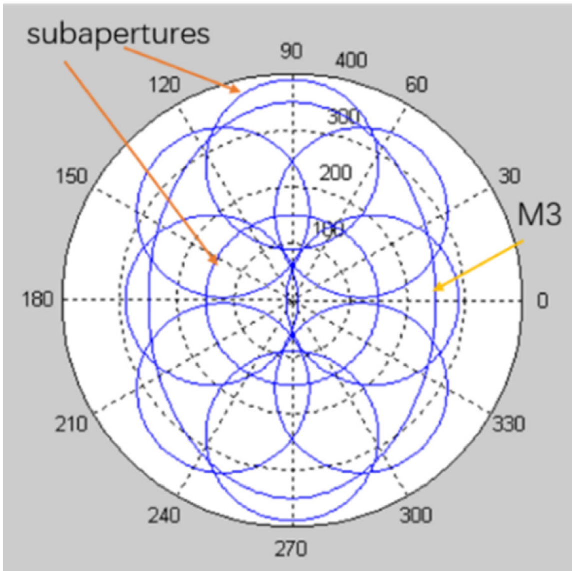

Fig. 6. Subaperture distributions.

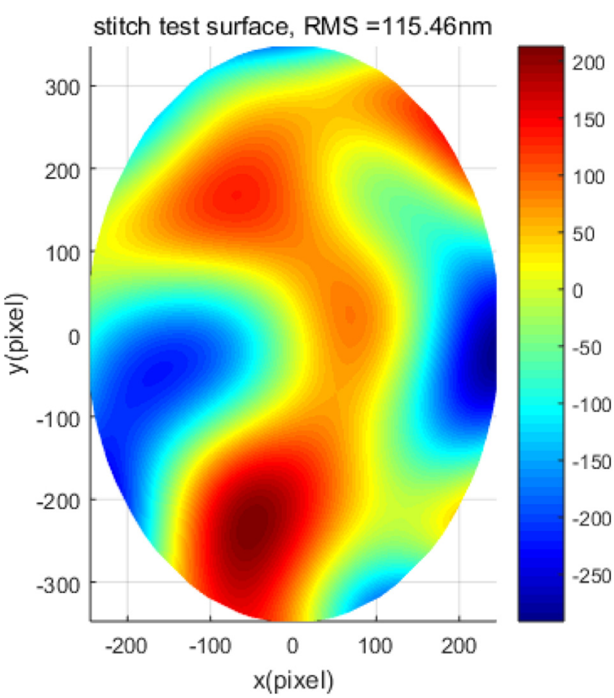

Fig. 7. Stitching map of M3.

$$Q_{rr}=\begin{bmatrix}\sum_{i=1}^{N}Z_{r5}Z_{r5} & \sum_{i=1}^{N}Z_{r5}Z_{r6} & \cdots & \sum_{i=1}^{N}Z_{r5}Z_{rm}\\ \sum_{i=1}^{N}Z_{r6}Z_{r5} & \sum_{i=1}^{N}Z_{r6}Z_{r6} & \cdots & \sum_{i=1}^{N}Z_{r6}Z_{rm}\\ \vdots & \vdots & \ddots & \vdots\\ \sum_{i=1}^{N}Z_{rm}Z_{r5} & \sum_{i=1}^{N}Z_{rm}Z_{r6} & \cdots & \sum_{i=1}^{N}Z_{rm}Z_{rm}\end{bmatrix} \tag{21}$$

$$Q_{tt}=\begin{bmatrix}\sum_{i=1}^{N}Z_{t5}Z_{t5} & \sum_{i=1}^{N}Z_{t5}Z_{t6} & \cdots & \sum_{i=1}^{N}Z_{t5}Z_{tm}\\ \sum_{i=1}^{N}Z_{t6}Z_{t5} & \sum_{i=1}^{N}Z_{t6}Z_{t6} & \cdots & \sum_{i=1}^{N}Z_{t6}Z_{tm}\\ \vdots & \vdots & \ddots & \vdots\\ \sum_{i=1}^{N}Z_{tm}Z_{t5} & \sum_{i=1}^{N}Z_{tm}Z_{t6} & \cdots & \sum_{i=1}^{N}Z_{tm}Z_{tm}\end{bmatrix} \tag{22}$$

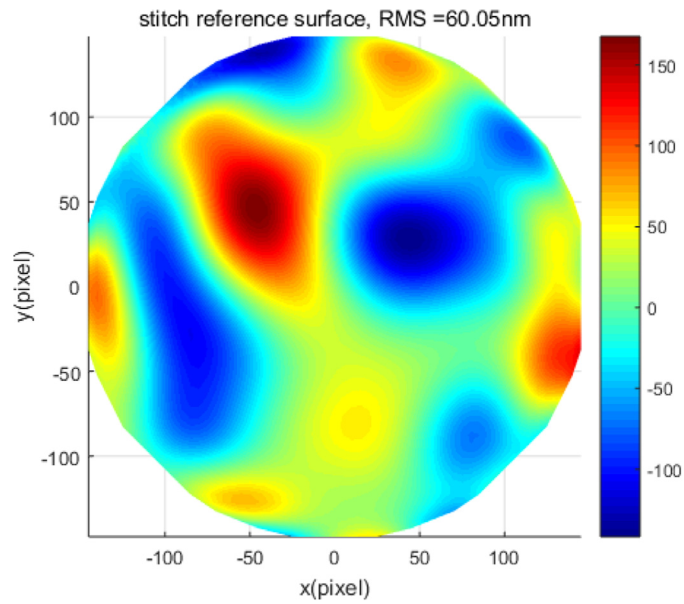

Fig. 8. Stitching map of the reference surface.

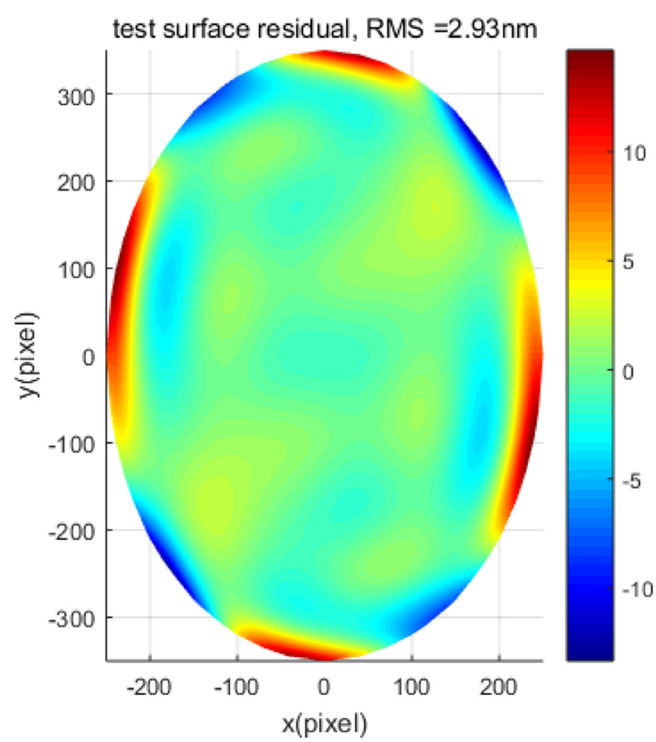

Fig. 9. Residual map of M3.

$$Q_{rt}=\begin{bmatrix}\sum_{i=1}^{N}Z_{r5}Z_{t5} & \sum_{i=1}^{N}Z_{r5}Z_{t6} & \cdots & \sum_{i=1}^{N}Z_{r5}Z_{tm}\\ \sum_{i=1}^{N}Z_{r6}Z_{t5} & \sum_{i=1}^{N}Z_{r6}Z_{t6} & \cdots & \sum_{i=1}^{N}Z_{r6}Z_{tm}\\ \vdots & \vdots & \ddots & \vdots\\ \sum_{i=1}^{N}Z_{rm}Z_{t5} & \sum_{i=1}^{N}Z_{rm}Z_{t6} & \cdots & \sum_{i=1}^{N}Z_{rm}Z_{tm}\end{bmatrix} \tag{23}$$

$R$is a vector with $[(rm+tm-8)+4N]$rows and can be written as:

$$R_i=\begin{bmatrix}a_{1i}\\ a_{2i}\\ a_{3i}\\ a_{4i}\end{bmatrix}(i=1\cdots N)\ R_t=\begin{bmatrix}a_{t5}\\ a_{t6}\\ \vdots\\ a_{tm}\end{bmatrix}R_r=\begin{bmatrix}a_{r5}\\ a_{r6}\\ \vdots\\ a_{rm}\end{bmatrix} \tag{24}$$

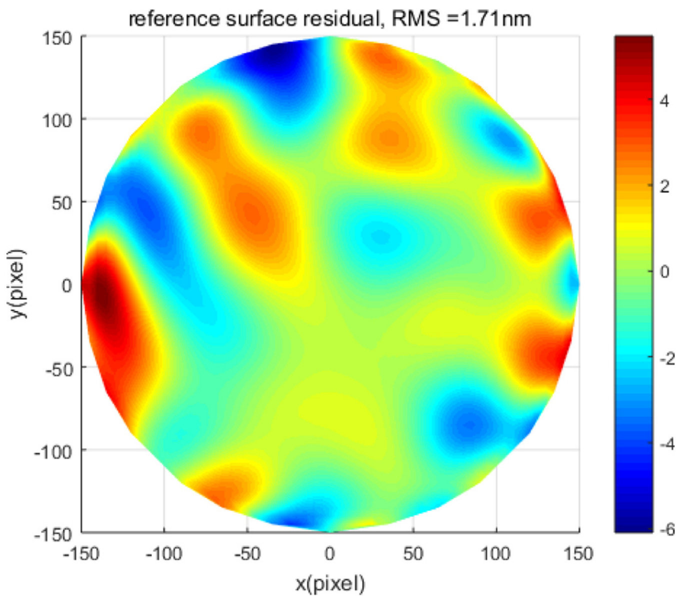

Fig. 10. Residual map of reference surface.

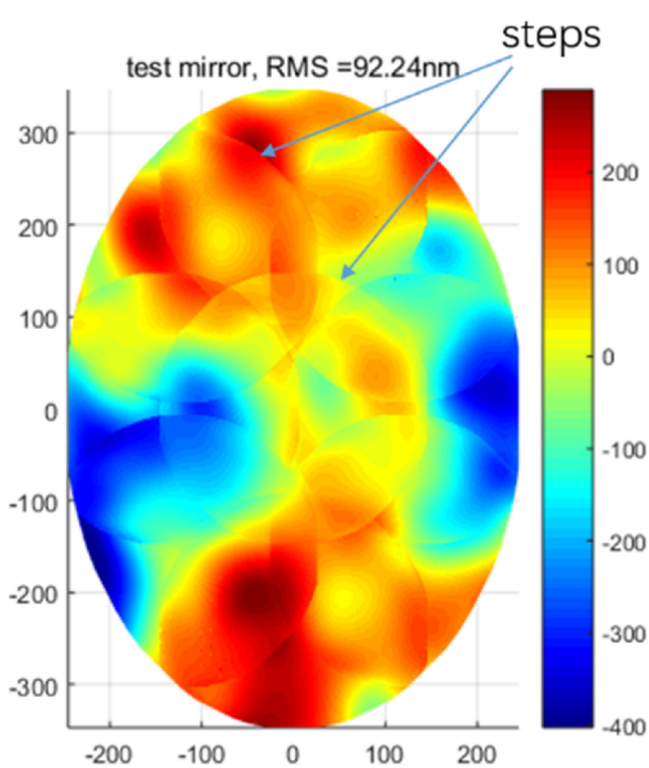

Fig. 11. Stitching map of M3 using the traditional method.

Table 2
Details of 5-dof platform.

Axis	Range of movement	Accuracy
X	1000 mm	0.01 mm
Y	500 mm	0.01 mm
Z	800 mm	0.02 mm
A	90°	4″
C	360°	10″

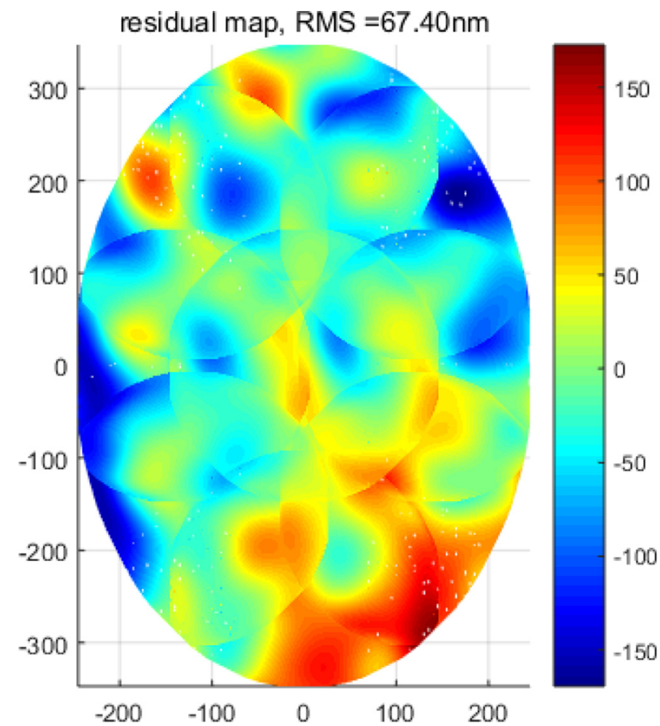

Fig. 12. Residual map of M3 using the traditional method.

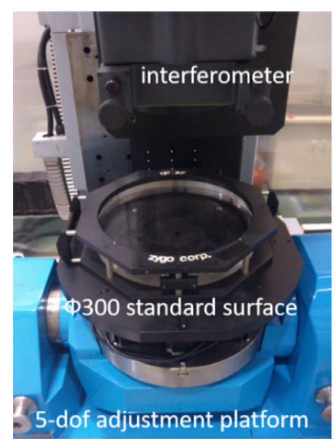

Fig. 13. Experimental setup.

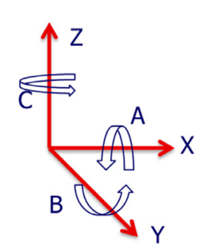

Fig.14. Description of 5-dof platform.

The coefficients $a_r$and $a_t$can be calculated from Eqs. (15)–(24). After determining the fitting coefficients, the maps of both the testing surface and the reference surface can be obtained.

3. Simulation

We ran simulations to demonstrate our proposed method. The simulations are based on the TMT (Thirty-Meter Telescope) project. The

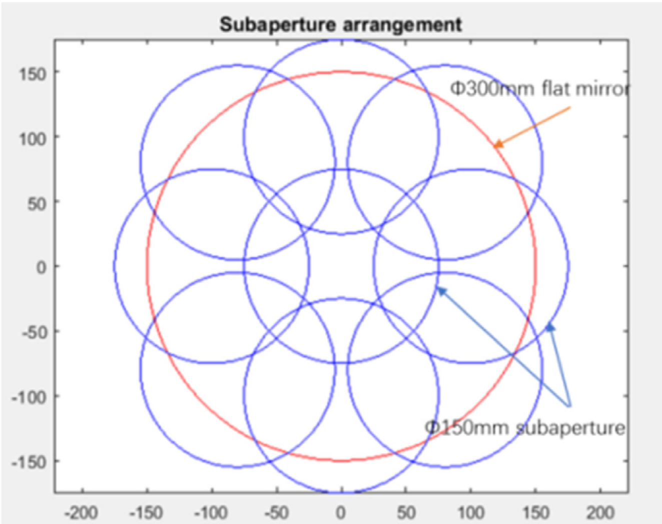

Fig. 15. Subaperture arrangement.

tertiary mirror in this project is an elliptical aperture mirror with dimensions 2.5 m × 3.5 m. The test setup is shown in Fig. 2.

In Fig. 2, the off-axis paraboloid (OAP) is an off-axis paraboloid reflective surface; M3 is an elliptical aperture testing surface with dimensions of 2.5 m × 3.5 m; the green part labeled as the test plate is a circular reference surface whose diameter is 1.5 m. The interferometer emits a standard spherical wavefront to the OAP mirror, which collimates the beam. The collimated beam, which is now a 1.5 m diameter beam, reflects off the reference and M3 and returns to the interferometer

The equipment to test M3 is shown in Fig. 3. The interferometer hangs at the top of the tower. M3 is placed on the swivel table, and can be moved around the swivel table and along the guideway.

According to the actual testing conditions, the parameters and errors in the testing simulation are listed in Table 1.

The detailed description of each error in Table 1 is as follows. Surface error of the reference surface means that the reference cannot be treated as perfect, and the RMS of the surface is 60.32 nm; Surface error of M3 describes the surface map of the tested surface. Alignment error in the radial direction ρ indicates the position error along the guideway when the mirror is moved along the guideway. Alignment error in the rotation direction θ is the angle error when the mirror is rotated around the swivel table. Tip error in the X direction, Tilt error in the Y direc-

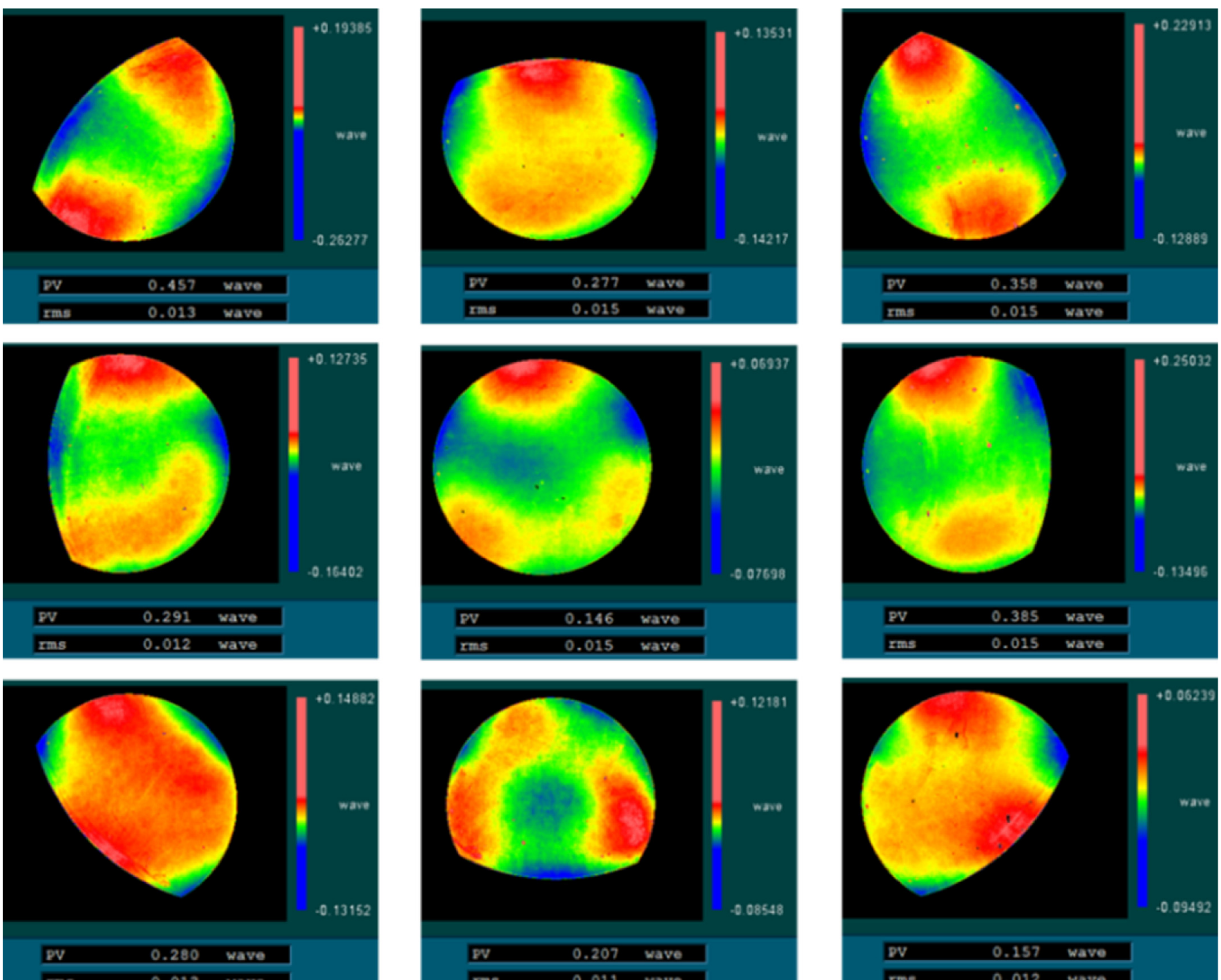

Fig. 16. Measured subapertures (wave= 632.8 nm).

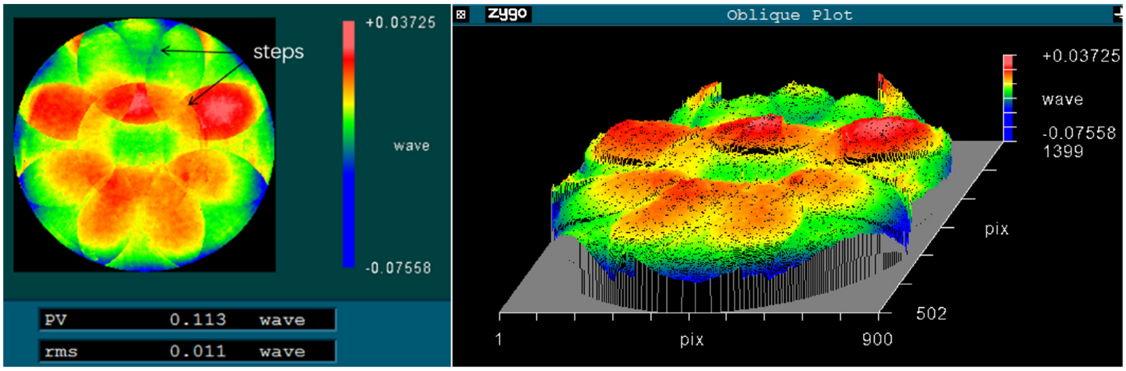

Fig. 17. Stitching result with traditional algorithm (wave= 632.8 nm).

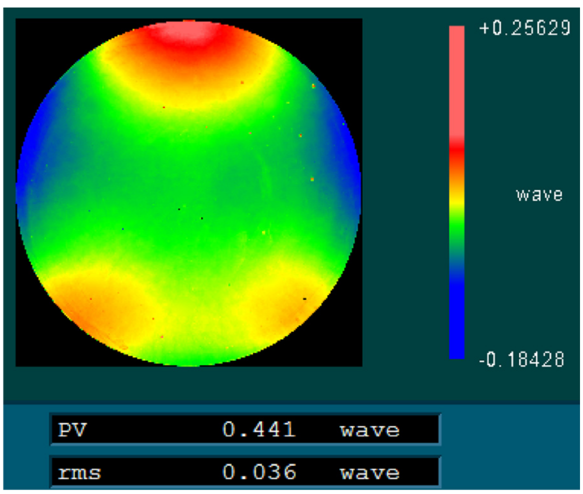

Fig. 18. Stitching map of Φ300 mm flat mirror with orthogonal fitting stitching algorithm (wave = 632.8 nm).

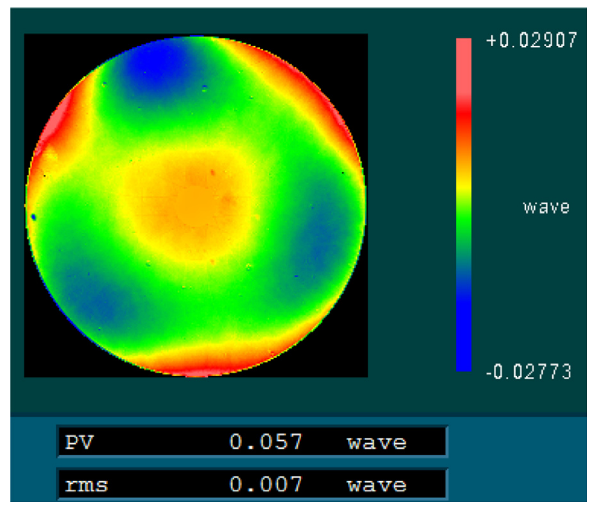

Fig. 19. Reference map with orthogonal fitting stitching algorithm (wave = 632.8 nm).

tion, and Mechanical jump indicate tip, tilt, and piston errors between subapertures, respectively. Random error in the map testing is a random surface error caused by the testing environment. Corresponding to Table 1, the surface errors of the reference surface and M3 are shown in Figs. 4 and 5, respectively.

The units of the X and Y axes in Figs. 4 and 5 are both in pixels. Each pixel represents 5 mm. The units of the Z axis in Figs. 4 and 5 are nanometer. To accomplish the stitching testing, nine subapertures are specified, as shown in Fig. 6.

After applying our proposed algorithm to the subaperture testing maps, the map of M3 was obtained, as shown in Fig. 7.

The reference map shown in Fig. 8 is calculated at the same time.

The units of X and Y in Figs. 7 and 8 are both in pixels. Each pixel also represents 5 mm. The units of Z in Figs. 7 and 8 are nm. To verify the stitching accuracy, the residual maps for both M3 and the reference surface were derived by subtracting the data between the stitching map and original map point by point, as shown in Figs. 9 and 10, respectively.

All X, Y, and Z units are the same as in previous figures. Figs. 9 and 10 show that the RMS of the M3 residual map is 2.93 nm, while the RMS of the residual map of the reference surface is 1.71 nm, which proves that stitching maps are consistent with the original maps for both the M3 and the reference surface. To compare the stitching results between the traditional stitching algorithm [14] and our orthonormal polynomial fitting algorithm, the stitching was also taken using the traditional method, and the stitching map of M3 is shown in Fig. 11 while the relative residual map of M3 is shown in Fig. 12.

All units in the two figures are those previously specified. Figs. 11 and 12 show that obvious steps can be observed at the edges of the subapertures, while there are no steps in either the stitching map or the residual map calculated with our proposed method, which means that our stitching map is smooth and continuous. The RMS error of the residual map in Fig. 12 is 67.4 nm, which indicates that the reference surface error cannot be ignored anymore in the stitching, as would be the case using the traditional stitching method. At the same time, from the stitching results in Figs. 7–10, it can be seen that stitching can be accomplished with our proposed orthonormal polynomial fitting algorithm very well.

4. Experiment

An experiment was carried out to validate the accuracy of the above orthogonal fitting stitching algorithm based on current equipment in the laboratory. In the experiment, a Zygo standard surface with Φ300 mm aperture was tested with a Φ150 mm interferometer and a five-degrees of freedom (5-dof) adjustment platform including the X, Y, Z, A and C axis, as shown in Figs. 13 and 14. The range of movement and relative accuracy of each axis can be found in Table 2. As the verification experiment, nine subapertures were measured with the interferometer. The arrangement of subapertures is shown in Fig. 14 and the subaperture testing results are shown in Fig. 15.

To further illustrate the advantage of the orthogonal fitting stitching algorithm, we compared the stitching results between the traditional stitching algorithm [14] and the orthogonal fitting stitching algorithm.

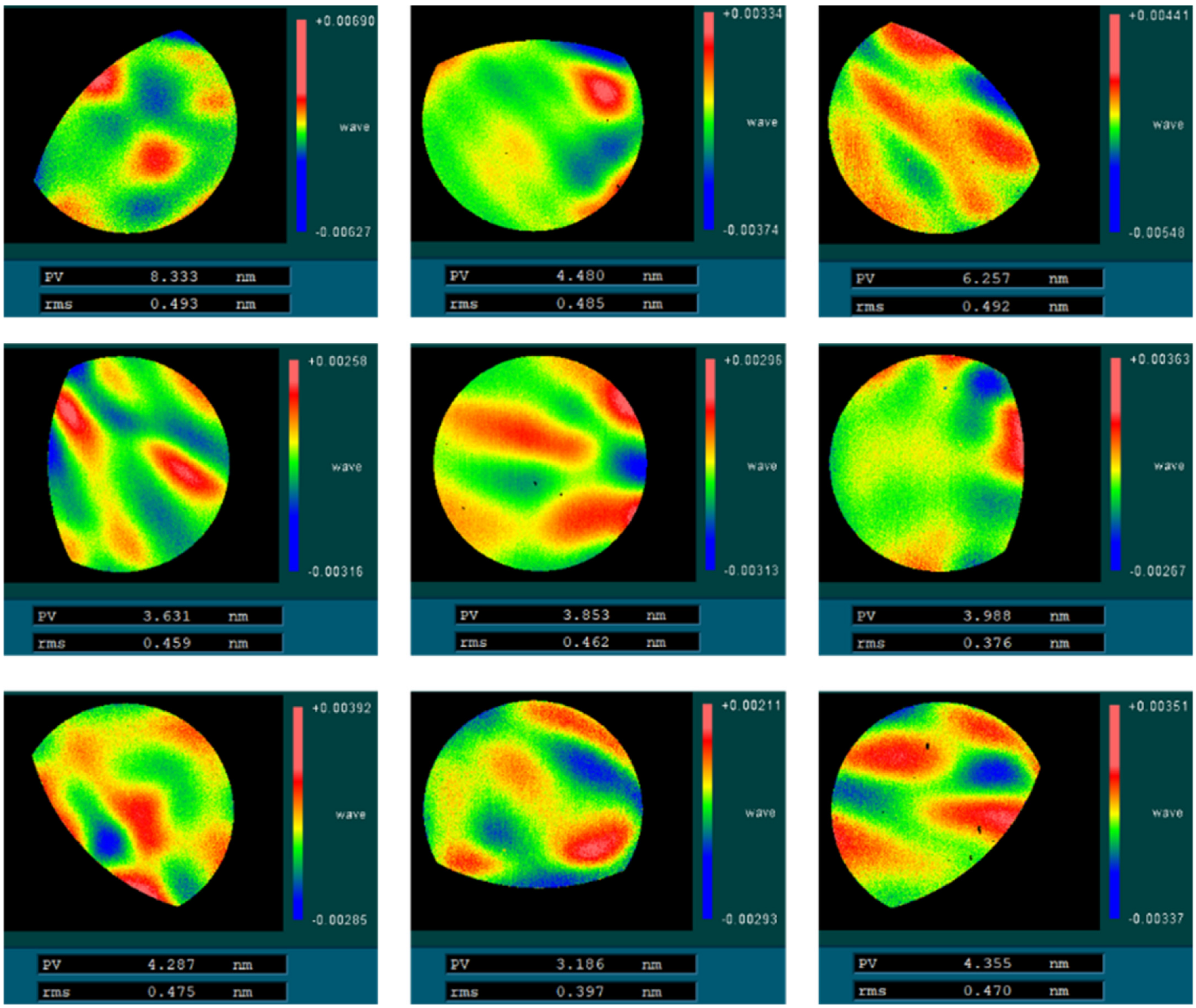

Fig. 20. Difference maps between each subaperture map and corresponding stitching map (after both the reference map and alignment terms are subtracted from the difference map).

Fig. 17 shows the stitching result with the traditional stitching algorithm [14], which accomplishes stitching by removing the relative adjustment errors between subapertures using the least squares method. Obvious steps appeared at the edges of the overlapping areas between adjacent subapertures. As assumed in the traditional stitching algorithm, compared with the testing mirror, the surface error of the interferometer standard lens is so small that it can be ignored in the subaperture testing. In this case, the method of calculating stitching coefficients in the traditional stitching algorithm can be used to evaluate the differences between subapertures, and stitching can be accomplished very well.

However, in the above experiment, the surface error of the interferometer standard lens was not negligible compared to the subaperture error of the testing mirror. Figs. 18 and 19 show the stitching maps of the Φ300 mm flat mirror and the reference surface maps of the interferometer standard lens using the orthogonal fitting stitching algorithm calculation, respectively. The peak-to-valley (PV) and RMS errors of the testing map are 0.441λ and 0.036λ, respectively while the PV and RMS errors of the reference map are 0.057λ and 0.007λ, respectively ($\lambda = 632.8$ nm). From Figs. 18 and 19, it is evident that both the reference map and the testing map can be tested at the same time with the orthogonal fitting stitching algorithm.

To further evaluate the performance of our stitching method, we calculated the difference maps between each subaperture data and the stitching map (both the reference map and alignment terms are subtracted from the difference map). The difference maps are an important indicator of the stitching quality and are shown in Fig. 20. It can be seen from Fig. 20 that the RMS of each difference map is within 0.5 nm, which verifies the capability of our stitching method.

The pixel-wise subaperture variations after the reference map and relative alignment are removed were also analyzed as follows. Fig. 21 indicates that the maximum RMS of subaperture variations between adjacent subapertures in the overlapped areas is 0.24 nm. This verifies the consistency of adjacent subaperture testing maps in the overlapping area (after the reference map and relative alignment are removed). The stitching results are excellent, and demonstrate the powerful capabilities of our stitching method.

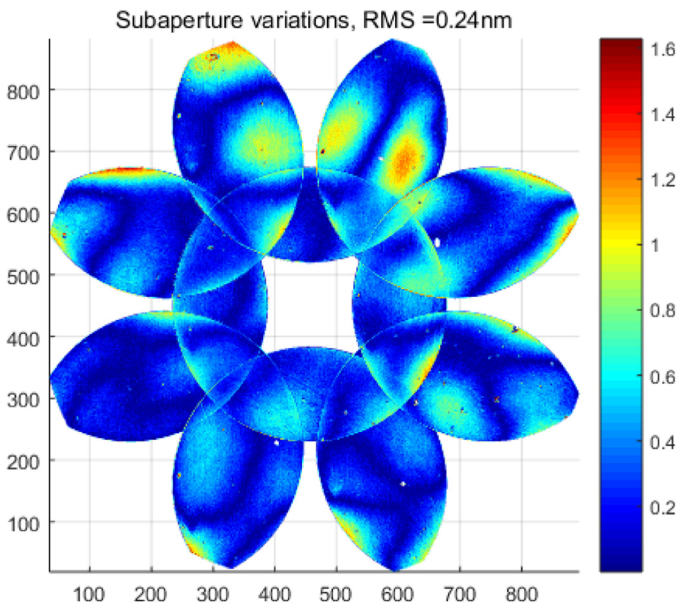

Fig. 21. Subaperture variations.

5. Conclusion

We propose an orthogonal fitting stitching algorithm to measure flat mirror surfaces when considering the errors of the reference surface. With the proposed stitching algorithm, both the reference surface and the testing surface can be calculated together. From both the M3 testing simulation and the experimental results, it is evident that the reported method can obtain the reconstructed full-aperture surface map and the reference surface map simultaneously with satisfactory accuracy. As the orthogonal fitting stitching algorithm is now fully developed to accomplish the absolute measurement of flat mirrors with large apertures, further research is needed for the absolute measurement of more complex surfaces such as convex aspherical mirrors and freeform surfaces.

Acknowledgments

We would like to thank the National Natural Science Foundation of China (61805089); Science and Technology Program of Shenzhen (No. JCYJ20160531194407693) and National Natural Science Foundation of China (61775067) for financial support.

References

[1] Skidmore W. Thirty meter telescope detailed science case: 2015. RAA 2015;15(12):1945–2140.
[2] Li HY, Walker D, Yu GY, Zhang W. Modeling and validation of polishing tool influence functions for manufacturing segments for an extremely large telescope. Appl Opt 2013;52(23):5781–7.
[3] Ma DL. Recommended conceptual optical system design for China's Large Optical-infrared Telescope (LOT). Opt Express 2018;28(1):108–19.
[4] Wen YF, Cheng HB, Tam HY, Zhou DM. Modified stitching algorithm for annular subaperture stitching interferometry for aspheric surfaces. Appl Opt 2013;52(23):5686–94.
[5] Hou X, Wu F, Yang L, Chen Q. Experimental study on measurement of aspheric surface shape with complementary annular subaperture interferometric method. Opt Express 2007;15(20):12890–9.
[6] Liu YM, Lawrence GN, Koliopoulos CL. Subaperture testing of aspheres with annular zones. Appl Opt 1988;27(21):4504–13.
[7] Chen SY, Xue S, Dai YY, Li SY. Subaperture stitching test of large steep convex spheres. Opt Express 2015;23(22):29047–58.
[8] Zhao ZX, Zhao H, Gu FF, Du HB, Li KX. Non-null testing for aspheric surfaces using elliptical sub-aperture stitching technique. Opt Express 2014;22(5):5512–20.
[9] Kulawiec A, Murphy P, Marco MD. Measurement of high-departure aspheres using subaperture stitching with the Variable Optical Null (VONTM). Proc SPIE 2010;7655(765512):1–4.
[10] Thunen JG, Kwon OY. Full aperture testing with subaperture test optics. Proc SPIE 1982;351:19–27.
[11] Chow WW, Lawrence GN. Method for subaperture testing interferogram reduction. Opt Lett 1983;8(9):468–70.
[12] Stuhlinger TW. Subaperture optical testing: experimental verification. Proc SPIE 1986;656:118–27.
[13] Otsubo M, Okada K, Tsujiuchi J. Measurement of large plane surface shapes by connecting small-aperture interferograms. Opt Eng 1994;33:608–13.
[14] Yan LS, Wang XK, Zheng LG, Zeng XF, Hu HX, Zhang XJ. Experimental study on subaperture testing with iterative triangulation algorithm. Opt Express 2013;21(19):22628–44.
[15] Zhao CY, Burge JH. Stitching of off-axis sub-aperture null measurements of an aspheric surface. Proc SPIE 2008;7063(706316):1–7.
[16] QED Technologies Inc., "Software patent: simultaneous self-calibrated subaperture stitching for surface figure measurement (interferometer)," European patent EP 1,324,006 (1 July 2003).
[17] Tian C, Yang YY, Wei T, Zhuo YM. Nonnull interferometer simulation for aspheric testing based on ray tracing. Appl Opt 2011;50(20):3559–69.
[18] Zhang L, Liu D, Shi T, Yang YY, Chong SY, Ge BL, Shen YB, Bai J. Aspheric subaperture stitching based on system modeling. Opt Express 2015;23(15):19176–88.
[19] Liu D, Yang YY, Tian C, Luo YJ, Wang L. Practical methods for retrace error correction in nonnull aspheric testing. Opt Express 2009;17(9):7025–35.
[20] Su P, Burge JH, Parks RE. Application of maximum likelihood reconstruction of subaperture data for measurement of large flat mirrors. Appl Opt 2010;49(1):21–31.
[21] Virendra NM, Dai GM. Orthonormal polynomials in wavefront analysis: analytical solution. J Opt Soc Am A 2007;24(9):2294–3016.
[22] Dai GM, Virendra NM. Nonrecursive determination of orthonormal polynomials with matrix formulation. Opt Lett 2007;32(1):76 74.
[23] Golub GH, Vanloan CF. Matrix computations. 3rd ed. Johns Hopkins University; 1996.